Adjustable Positive-Negative Signal in Self-Driven Photodetector based on Cubic $CH_3NH_3PbI_3$ Large Single Crystal

Xuewei Fu,[a] Yunying Wang,[a] Huawei Zhou,[a,*] Yan Chen,[a] Chen Wang,[a] Xingchen Hu,[a] Yi Wang,[a] Jie Yin,[a,*] and Xianxi Zhang[a,*]

Received (in XXX, XXX) Xth XXXXXXXXX 20XX, Accepted Xth XXXXXXXXX 20XX
DOI: 10.1039/b000000x

In this study, for the first time, self-driven photodetector based on cubic $CH_3NH_3PbI_3$ large single crystal (C-$MAPbI_3$ LSC) with adjustable positive-negative signal is fabricated. The preparation of $MAPbI_3$ large single crystal ($MAPbI_3$ LSC) is realized by the method of growth-drop-growth (GDG). The band gap of $MAPbI_3$ single crystals with Pm-3m (221) space group (6.134×6.134×6.134 Å, 90.00 x 90.00 x 90.00) is 1.58 eV. $CH_3NH_3^+$ cation is orientation-disorder within the perovskite cubo-octahedral cavity. The photocurrent density at 803 nm of the C-$MAPbI_3$ LSC photodetector under different bias voltages is the highest under different wavelength. The responsivities (R), response time, external quantum efficiencies (EQE) and the detectivity (D) for C-$MAPbI_3$ LSC photodetector at 803 nm wavelength with 1 W m^{-2}, respectively, is 508.7 μA/mW, 0.1338 ms, 79.6% and $8.64*10^{11}$ Jones. Notably, the C-$MAPbI_3$ LSC photodetector can be self-driven under 0 V bias voltage, in particular, the positive and negative values of the photocurrent can be adjusted. The proposed mechanism of poling inducing built-in potential is explained adjustable positive-negative signal in self-driven photodetector based on cubic $CH_3NH_3PbI_3$ large single crystal.

In recent years, various types of perovskite photodetectors have been developed rapidly due to their excellent light harvesting performance. Among them, there are many studies on photodetectors based on $CH_3NH_3PbI_3$ ($MAPbI_3$) perovskite materials, and there are roughly the following types. The first type is polycrystalline perovskite film photodetectors with different morphology. For example, Yin Zhang, Juan Du[1] and their partners developed photodetectors based on island-structured $CH_3NH_3PbI_3$ thin films; S. Tong, H. Wu[2] and their partners developed photodetectors based on polycrystalline $CH_3NH_3PbI_3$ films by in-situ thermal-treatment doctor blading technique in ambient condition (humidity ~45%). The second type is a variety of heterojunction photodetectors. For example, Huayan Xia, Sichao Tong[3] and their partners developed perovskite network photodetectors based on $CH_3NH_3PbI_3$/C8BTBT bulk heterojunction; Yafei Wang, Ting Zhang[4] and their partners developed $CH_3NH_3PbI_3$/PCBM heterojunction photodetectors through an anti-solvent process. In addition, there are $CH_3NH_3PbI_3$/C60[5] and solution processed $CH_3NH_3PbI_3/SnO_2$[6] heterojunction photodetectors. The third type is photodetectors with single crystal particles. For example, Xiang Qin, Yifan Yao[7] and their partners developed $CH_3NH_3PbI_3$ crystals with the morphologies of nanowires and nanoplates via a simple solution immersing method and used them to prepare photodetectors. In addition, transparent and flexible photodetectors[8] (PDs) based on $CH_3NH_3PbI_3$ perovskite and photodetectors based on 2D[9] or 1D[10] hybrid organic-inorganic perovskite (i.e., $CH_3NH_3PbI_3$) nanocrystals were developed.

However, the photodetector based on cubic $CH_3NH_3PbI_3$ large single crystal (C-$MAPbI_3$ LSC), in particular, adjustable the positive and negative values of the photocurrent, to date, is not reported. In this study, for the first time, self-driven photodetector based on cubic $CH_3NH_3PbI_3$ large single crystal (C-$MAPbI_3$ LSC) with adjustable positive-negative signal are fabricated.

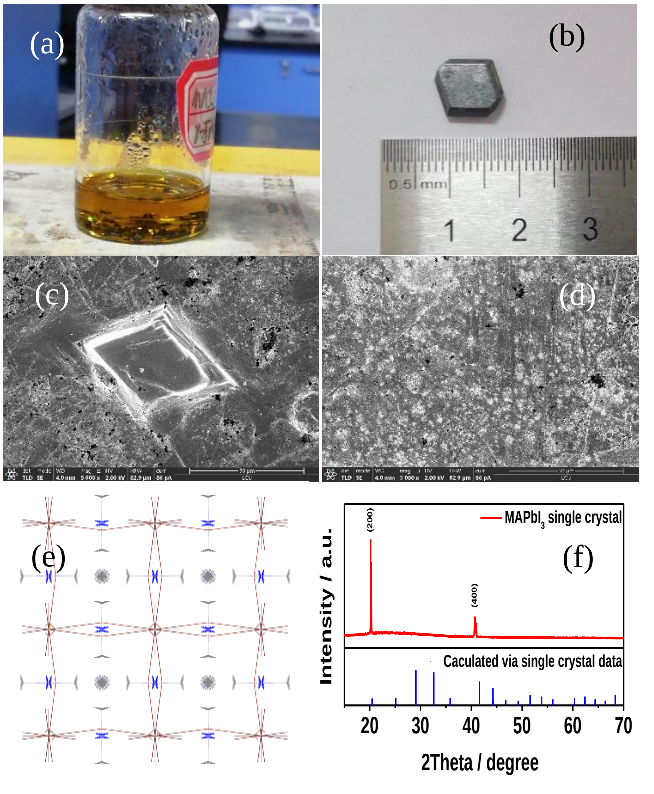

Figure 1: (a) Photo of the $MAPbI_3$ crystal seeds in γ-GBL; (b) Photo of the $MAPbI_3$ large single crystal via growth-drop-growth method; (c) SEM image of the surface of unpolished $MAPbI_3$ large single crystal; (d) SEM image of the surface of polished $MAPbI_3$ large single crystal; (e) Crystal structure diagram of cubic $MAPbI_3$; (f) X-ray Diffraction pattern of C-$MAPbI_3$ SC prepared by GDG and calculated via single crystal data.

The photo of the $MAPbI_3$ crystal seeds prepared by the modified inverse temperature crystallization method is shown in the Figure 1a. The preparation of $MAPbI_3$ large single crystal

($MAPbI_3$ LSC) is realized by the method of growth-drop-growth (GDG). Detailed experimental process are listed in the experimental section. A photo of $MAPbI_3$ LSC is shown in Figure 1b. The size of $MAPbI_3$ LSC reaches centimeter level. The surface topography of the unpolished $MAPbI_3$ LSC was characterized by scanning electron microscope (SEM), as shown in Figure 1c. The large convex crystalline grains are observed on $MAPbI_3$ LSC surface, which will affect the conductivity of the interdigital gold electrode and further affect the collection of photoelectrons. Therefore, the surface of the $MAPbI_3$ LSC is smoothed by mechanical polishing, and the polished surface is very flat and uniform, as shown in Figure 1d. The crystal structure of $MAPbI_3$ crystal seeds is solved by Shelxtl software. From the single crystal diffraction data, we can know that: $MAPbI_3$ single crystal has a cubic phase with Pm-3m (221) space group (6.134×6.134×6.134 Å, 90.00 x 90.00 x 90.00). Figure 1e shows the schematic diagram of the crystal structure of $MAPbI_3$. $CH_3NH_3^+$ cation is orientation-disorder within the perovskite cubo-octahedral cavity. The detailed crystal structure information is listed in Table S1-S6. The X-ray diffraction patterns of C-$MAPbI_3$ SC prepared by GDG and calculated via single crystal data with Diamond software is shown in Figure 1f. The peaks appear at 20.17 and 40.72 degree, which correspond to (200) and (400) crystal planes, respectively.

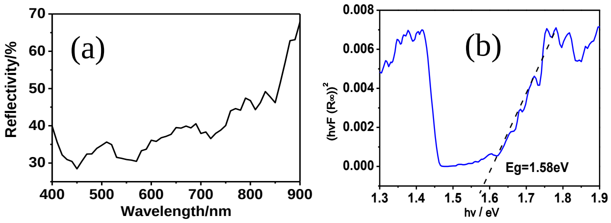

Figure 2. (a) Diffuse Reflectance Spectra of C-$MAPbI_3$ LSC; (b) hv-(hvF(R∞))^2 curve of C-$MAPbI_3$ LSC.

The optical properties of C-$MAPbI_3$ LSC were characterized by diffuse reflectance spectroscopy as shown in Figure 2a. To calculate the band gap of C-$MAPbI_3$ LSC, the diffuse reflectance spectrum is converted to Kubelka-Munk spectrum. The results indicate that the band gap of C-$MAPbI_3$ LSC is 1.58 eV, as shown in Figure 2b.

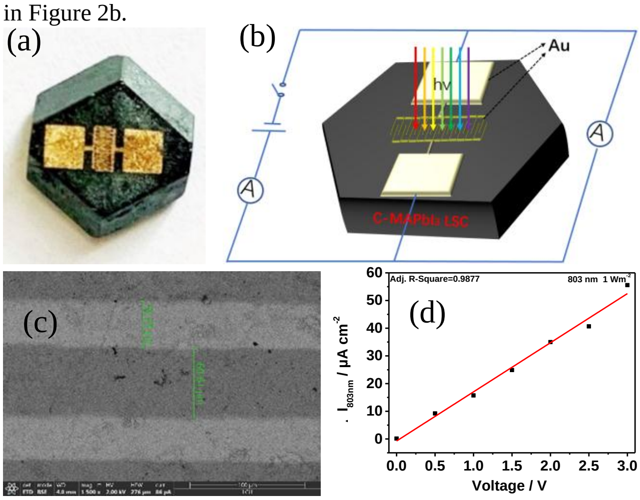

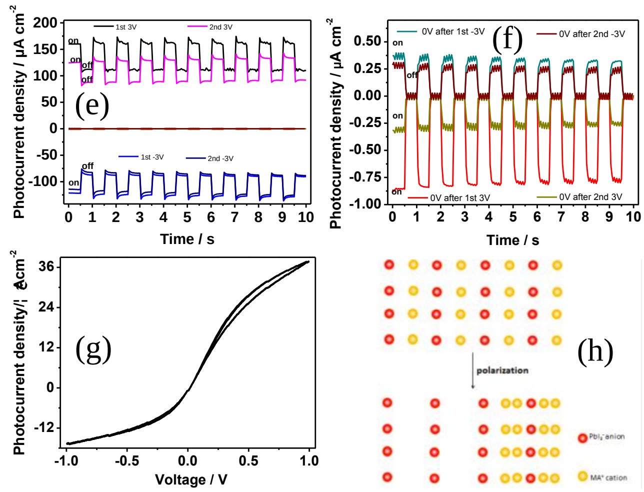

Figure 3. (a) Photo of C-$MAPbI_3$ LSC after evaporating interdigital gold electrode; (b) Model diagram of the photodetector based on C-$MAPbI_3$ LSC; (c) SEM image of the surface of C-$MAPbI_3$ LSC after evaporating interdigital gold electrode; (d) A linear fitted line of $\triangle I_{803\ nm}$ -bias voltage; (e) and (f) Photocurrent density−time curve of the photodetector based on C-$MAPbI_3$ LSC after applying positive and negative bias voltage under 803 nm wavelength with 1 W m^{-2} light intensity; (g) Hysteresis characteristics of photodetector based on C-$MAPbI_3$ LSC measured from 0 to 1 V with 500 mV s^{-1}; (h) Diagram of voltage inducing migration of ion in the photodetector based on C-$MAPbI_3$ LSC.

Photo and model diagram of C-$MAPbI_3$ LSC after evaporating interdigital gold electrode, respectively, is shown in Figure 3a and 3b. The width of the interdigital gold electrode and photodetector is 40 μm, and 60 μm, respectively, as shown in SEM in Figure 3c. To study the photoelectric performance of the photodetector based on C-$MAPbI_3$ LSC, we evaluated the response of photocurrent density at different wavelengths through continuous illumination and linear scanning voltage (where 678 nm was measured at 18 W m^{-2}, 922 nm at 20 W m^{-2}, 957 nm at 25 W m^{-2} and 975 nm at 28 W m^{-2}, other wavelength at 30 W m^{-2}), and the results are shown in Figure S1. It can be seen that for any wavelength, the photocurrent increases as the voltage increases. We transformed Figure S1 into the photocurrent density-wavelength curve, as shown in Figure S2. At any voltage, the maximum photocurrent response is obtained at 803 nm. Different bias voltages were applied to the device at 803 nm wavelength with 1 W m^{-2} light intensity to research its periodicity. The photocurrent density-time curve (0, 0.5, 1, 1.5, 2, 2.5, and 3 V) is shown in Figure S3. The results show that $\triangle I_{803\ nm}$ ($\triangle I_{803\ nm} = I_{on} - I_{off}$, 803 nm is the wavelength, I_{on} and I_{off}, respectively, represents the photocurrent density under the light radiation and the dark state) increases as the increase of bias voltage. According to the regularity, the $\triangle I_{803\ nm}$ -bias voltage curve is plotted and linear fitted as shown in Figure 3d. The correlation coefficient is 0.9877, which indicates that they have good linear relationship. Besides, the value of $\triangle I_{803\ nm,\ 3V}$ reach to 55.28 μA cm^{-2} from 0.85 μA cm^{-2} at 0V, which indicates that the sensitivity for weak light (1 W m^{-2}) is significantly improved. Meanwhile, we calculated the responsivities (R), external quantum efficiencys (EQE) and the detectivity (D) of C-$MAPbI_3$ LSC photodetector under 3 V bias voltage and 803 nm wavelength with 1 W m^{-2} light intensity using data in Figure 3S. By substituting the data into following formulas (Equ.1 to 3), R=508.7 μA/mW, EQE=79.6 % and D=8.64*10^{11} Jones can be obtained.

$$R = \frac{I_{PC} - I_{Dark}}{P \times S} \quad \text{(Equ.1)}$$

$$\mathrm{EQE} = \frac{R \times hc}{e\lambda} \quad \text{(Equ.2)}$$

and $$D = \frac{R}{(2e \times I_{Dark})^{\frac{1}{2}}} \quad \text{(Equ.3)}$$

In the above formulas, I_{PC} and I_{Dark} are photocurrents of the photodetector with and without illumination, respectively. P is the light intensity. S is the effective area of the photodetector. C stands for light speed and λ is the wavelength of light source. Response times, as shown in Figure S4, of the C-$MAPbI_3$ LSC is 0.1338 ms under 1 V bias potential and 803 nm with 1 Wm^{-2}.

In addition, we found that the C-$MAPbI_3$ LSC photodetector can be self-driven under 0 V bias voltage, in particular, the positive and negative values of the photocurrent can be adjusted, as shown in Figure 3e and 3f. After applying 3 V external bias voltage (poling), we tested the photoelectric response of the C-$MAPbI_3$ LSC photodetector under 0 V bias voltage. The photocurrent obtained at this time is negative. After applying -3 V bias voltage, we tested the photoelectric response of the photodetector under 0 V bias voltage. The photocurrent obtained at this time is positive. We know that perovskite material appears hysteresis phenomenon when it is used as solar cell. Figure 3g is the CV test of photodetector. The CV with other scanning speed is shown in the Figure S5-S8 in the supporting information. From these CV results, we can see that the hysteresis phenomenon appears in C-$MAPbI_3$ LSC photodetector in the process of applying bias voltage. In addition, the results of scanning 100 CV cycles, as shown in Figure S9-S11 show that the hysteresis phenomenon shows good repeatability. Its mechanism is shown in the Figure 3h: MA^+ cations transfer directionally under the action of bias voltage. Polarization occur inside C-$MAPbI_3$ LSC, which will form a built-in potential. The direction of the built-in potential inside C-$MAPbI_3$ LSC is opposite to that of bias voltage. The built-in potential drives the photoelectrons to move directionally. By changing the positive and negative values of bias potential, the direction of the built-in potential will be changed. The change in the direction of built-in potential changes the positive and negative values of the photocurrent.

Acknowledgements

This work was financially supported by the Shandong Province Natural Science Foundation (Grant No. ZR2019MB021).

Notes and references

[a]School of Chemistry and Chemical Engineering; College of Materials Science and Engineering; Shandong Provincial Key Laboratory/Collaborative Innovation Center of Chemical Energy Storage; Liaocheng University.

* E-mail: zhouhuaweiopv@163.com; yinjieily@163.com; xxzhang3@126.com.

1. Y. Zhang, J. Du, X. Wu, G. Zhang, Y. Chu, D. Liu, Y. Zhao, Z. Liang and J. Huang, *Acs Applied Materials & Interfaces*, 2015, **7**, 21634-21638.
2. S. C. Tong, H. Wu, C. J. Zhang, S. G. Li, C. H. Wang, J. Q. Shen, S. Xiao, J. He, J. L. Yang, J. Sun and Y. L. Gao, *Organic Electronics*, 2017, **49**, 347-354.
3. H. Y. Xia, S. C. Tong, C. J. Zhang, C. H. Wang, J. Sun, J. He, J. Zhang, Y. L. Gao and J. L. Yang, *Applied Physics Letters*, 2018, **112,** 5024330.
4. Y. F. Wang, T. Zhang, P. Zhang, D. T. Liu, L. Ji, H. Chen, Z. D. Chen, J. Wu and S. B. Li, *Organic Electronics*, 2018, **57**, 263-268.
5. Y. K. Wang, D. Z. Yang, X. K. Zhou, S. M. Alshehri, T. Ahamad, A. Vadim and D. G. Ma, *Organic Electronics*, 2017, **42**, 203-208.
6. H. R. Wu, Z. S. Su, F. M. Jin, H. F. Zhao, W. L. Li and B. Chu, *Organic Electronics*, 2018, **57**, 206-210.
7. X. Qin, Y. F. Yao, H. L. Dong, Y. G. Zhen, L. Jiang and W. P. Hu, *Chemistry-an Asian Journal*, 2016, **11**, 2675-2679.
8. J. Y. Liu, Y. Z. Xue, Z. Y. Wang, Z. Q. Xu, C. X. Zheng, B. Weber, J. C. Song, Y. S. Wang, Y. R. Lu, Y. P. Zhang and Q. L. Bao, *Acs Nano*, 2016, **10**, 3536-3542.
9. Y. Wang, Q. G. Song, T. Lin, Y. Fu, X. Sun, B. Chu, F. M. Jin, H. F. Zhao, W. L. Li, Z. S. Su and Y. T. Li, *Organic Electronics*, 2017, **49**, 355-359.
10. X. Zhang, C. C. Liu, G. Ren, S. Y. Li, C. H. Bi, Q. Y. Hao and H. Liu, *Nanomaterials*, 2018, **8,** 8050318.